Journal of Biomechanics 48 (2015) 930–940

Contents lists available at ScienceDirect

Journal of Biomechanics

journal homepage: www.elsevier.com/locate/jbiomech
www.JBiomech.com

Analysis and analytical characterization of bioheat transfer during radiofrequency ablation

Keyong Wang [a,b], Fatemeh Tavakkoli [b], Shujuan Wang [b], Kambiz Vafai [b,*]

[a] School of Mechanical Engineering, Shanghai University of Engineering Science, Shanghai 201620, China
[b] Department of Mechanical Engineering, University of California, Riverside, CA 92521, USA

ARTICLE INFO

Article history:
Accepted 15 February 2015

Keywords:
Boiheat transfer
Porous medium
Radiofrequency ablation
Biological tissue/organ
Local thermal non-equilibrium

ABSTRACT

Understanding thermal transport and temperature distribution within biological organs is important for therapeutic aspects related to hyperthermia treatments such as radiofrequency ablation (RFA). Unlike surface heating, the RFA treatment volumetrically heats up the biological media using a heating probe which provides the input energy. In this situation, the shape of the affected region is annular, which is described by an axisymmetric geometry. To better understand the temperature responses of the living tissues subject to RFA, comprehensive characteristics of bioheat transport through the annular biological medium is presented under local thermal non-equilibrium (LTNE) condition. Following the operational features of the RFA treatment, based on the porous media theory, analytical solutions have been derived for the blood and tissue temperature distributions as well as an overall heat exchange correlation in cylindrical coordinates. Our analytical results have been validated against three limiting cases which exist in the literature. The effects of various physiological parameters, such as metabolic heat generation, volume fraction of the vascular space, ratio of the effective blood to tissue conductivities, different biological media and the rate of heat exchange between the lumen and the tissue are investigated. Solutions developed in this study are valuable for thermal therapy planning of RFA. A criterion is also established to link deep heating protocol to surface heating.

1. Introduction

The modeling of bioheat transfer has been employed extensively in medical thermal therapeutic applications for predicting the temperature distribution (Khaled and Vafai, 2003; Khanafer and Vafai, 2009). Nowadays, cancer is still one of the lowest survival rate diseases. Hyperthermia treatment such as radiofrequency ablation (RFA) (Peng et al., 2011), microwave, laser (Dombrovsky et al., 2012), magnetic fluid (Giordano et al., 2010), etc. is recognized as the fourth adjunct cancer therapy technique following surgery, chemotherapy and radiation techniques. When biological tissues are subjected to high temperatures, which are typically 40–45 °C (Field, 1987), heat shock can cause a cancer cell to lose viability and eventually induce cell death (Kiss et al., 2009). In contrast to resection techniques, which have a poor prognostic outcome, RFA has the potential to improve and to optimize clinical treatment with fewer side effects (Goldberg et al., 2000; Peng et al., 2011). Similar to cryotherapy (Chua et al., 2007), RFA also has a minimally invasive nature. Briefly, RFA induces resistive heating in tissues in direct contact with an ablation electrode (Boronyak and Merryman, 2014). Liu (2001) presented an analytical solution to the Pennes bioheat transfer equation in three-dimensional geometry with practical hyperthermia boundary conditions and random heating. Chung and Vafai (2014) investigated analytically and numerically the effects of hyperthermia on low-density lipoprotein transport and heat transfer within a multi-layered arterial wall accounting for the fluid–structure interaction. However, the thermal responses of a living organ under ablation treatments have not yet been fully evaluated quantitatively in the clinical field. So it is imperative to study the general characteristics of bioheat transfer with medical affiliates in order to demonstrate the relationship between the heating power deposited in the tissue and the resulting tissue status post treatment.

A biological tissue consists of a microvascular bed with blood flow through many vessels. As such it is quite natural to treat the living tissue as a porous medium (Khaled and Vafai, 2003; Khanafer and Vafai, 2006; Zhang, 2009). Thus, the porous media theory can be utilized for bioheat transfer analysis, in which fewer assumptions are needed as compared to other established bioheat transfer models (Khaled and Vafai, 2003; Khanafer and Vafai, 2006, 2009; Nakayama and Kuwahara, 2008; Mahjoob and Vafai, 2009, 2010). Two primary models for analyzing heat transfer in a porous medium are: local thermal equilibrium (LTE) and local thermal non-equilibrium (LTNE). The LTE model is based on the assumption that the temperature for tissue phase is equal to that for blood phase, on a local basis, everywhere inside the porous medium. However, the LTE model does not hold for some physical

* Corresponding author.

http://dx.doi.org/10.1016/j.jbiomech.2015.02.023
0021-9290/

Nomenclature

a_{tb}	specific surface area (1/m)
Bi	Biot number, $h_{tb}a_{tb}H^2/k_{t,eff}$
c_b	blood specific heat (J/kg °C)
h_{tb}	blood–tissue interstitial heat transfer coefficient (W/m^2 °C)
H	heating penetration depth (m), R_o-R_i
k_b	blood thermal conductivity (W/m °C)
$k_{b,dis}$	blood dispersion thermal conductivity (W/m °C)
$k_{b,\mathrm{eff}}$	effective thermal conductivity of the blood phase (W/m °C)
k_t	tissue thermal conductivity (W/m °C)
$k_{t,eff}$	effective thermal conductivity of the tissue phase (W/m °C)
n	ratio of the heating probe to the annulus radii, R_i/R_o
Nu	Nusselt number at the probe–organ interface for LTNE model
q_w	imposed heat flux on the organ (W/m^2)
Q_{met}	metabolic heat generation within the biological tissue (W/m^3)
r	radial coordinate (m)
R_i	radius of the heating probe (m)
R_o	radius of the heated annulus (m)
T	temperature (°C)
$T_{b,m}$	blood bulk mean temperature (°C)
T_c	body core temperature (°C)
T_e	arterial blood temperature entering the organ (°C)
T_w	temperature of the probe–organ interface subject to an imposed heat flux (°C)
u	lumen velocity (m/s)
u_e	arterial blood velocity entering the organ (m/s)
z	axial coordinate (m)

Greek symbols

ε	porosity (volume fraction of the vascular space)
ζ	dimensionless position of the annulus regulated from 0 to 1, $\eta-\eta_i$
η	dimensionless radial coordinate, r/H
θ	dimensionless temperature, $k_{t,eff}(T-T_w)/q_wH$
$\theta_{b,m}$	dimensionless bulk mean blood temperature
θ_c	dimensionless body core temperature, $k_{t,eff}(T_c-T_w)/q_wH$
κ	ratio of the effective blood thermal conductivity to that of the tissue, $k_{b,eff}/k_{t,eff}$
λ	$=\sqrt{(1+\kappa)\mathrm{Bi}/\kappa}$
ξ	dimensionless axial coordinate, z/H
ρ_b	blood density (kg/m^3)
Φ	dimensionless heat generation within the biological tissue, $(1-\varepsilon)HQ_{met}/q_w$
ψ	ratio of the radius of the heating probe to the heating penetration depth, R_i/H

Subscripts/superscripts

b	blood phase
c	body core
i	inner surface of the heated annular region
o	outer surface of the heated annular region
t	tissue phase
w	probe surface

Symbol

$\langle\rangle$	intrinsic volume average of a quantity

situations when the temperature difference between the two phases is not negligible (Khaled and Vafai, 2003). In such cases, the LTNE model should be utilized to investigate the blood temperature changes as a result of tissue-blood convective heat exchange and blood perfusion (Xuan and Roetzel, 1997; Lee and Vafai, 1999; Alazmi and Vafai, 2000; Zhang, 2009; Mahjoob and Vafai, 2009, 2010; Rattanadecho and Keangin, 2013). Mahjoob and Vafai (2009) carried out a comprehensive investigation of bioheat transport through the tissue/organ incorporating hyperthermia treatment using LTNE, and had established exact solutions for the tissue and blood temperature profiles during surface heating.

In a separate work, Mahjoob and Vafai (2010) investigated characterization of bioheat transport through a dual layer biological media. Dombrovsky et al. (2013) conducted numerical simulations on laser-induced hyperthermia of superficial tumors. Keangin et al. (2013) highlighted the effects of electromagnetic field on biological materials. In their study, the coupled equations of electromagnetic wave propagation and heat transfer under the LTNE assumption were solved by the finite element method. Peng et al. (2011) presented a two-equation coupled bioheat model to investigate thermal energy exchange between the blood and its surrounding peripheral tissue. Zhang (2009) obtained dual-phase bioheat equations by analyzing non-equilibrium heat transfer in a living biological tissue. Most recently, Keangin and Rattanadecho (2013) investigated the transient distribution of tissue and blood temperatures inside a porous liver during microwave ablation process.

Analytical solutions in this area are very useful as they provide an effective route for parametric studies when a large number of variables are involved. Nevertheless, most of the existing analytical solutions are concentrated on surface heating in planar geometry. For deep hyperthermia treatments such as RFA, the heating domain is approximately an annulus. To the authors' knowledge, no work has been performed analytically in the open literature on heat transfer within an annular biological medium while incorporating the LTNE condition.

The present study aims at predicting the blood and tissue temperature distributions within biological media as well as heat transfer behavior during RFA. The influence of the pertinent parameters such as vascular volume fraction, the effective thermal conductivity ratio, metabolic heat generation, etc. is analyzed. A criterion is also constructed to bridge the bioheat transfer for deep heating such as RFA and that for surface heating (Mahjoob and Vafai, 2009, 2010) through a geometrical analysis.

2. Mathematical modeling

2.1. Problem description

Biological tissue generally contains blood vessels, cells and interstitial space (Mahjoob and Vafai, 2009), which can be categorized as vascular and extra-vascular regions, as shown in Fig. 1(a). As such, the whole anatomical structure can be modeled as a porous matrix through which the blood infiltrates. Generally, the pressure is uniformly higher throughout the tumor as compared to the peripheral values, which leads to an extremely slow interstitial flow inside the tumor (Wu et al., 2009). Hence, the blood flow within the tumor region can be represented by the Darcy flow model (Wu et al., 2009; Mahjoob and Vafai, 2009, 2010; Cookson et al., 2012). In this study, hydraulically and thermally fully developed condition is assumed. The flow is steady and incompressible. Natural convection and radiation

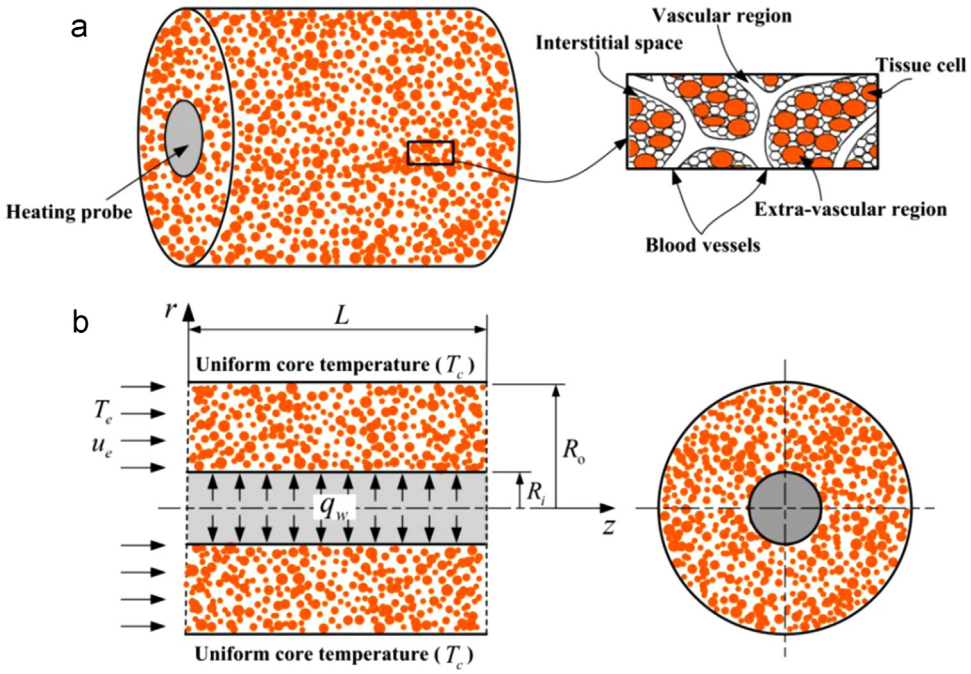

Fig. 1. Schematic diagram of (a) axisymmetric tissue-vascular system, and (b) model description for the radiofrequency ablation.

are negligible and thermodynamic properties of the blood and tissue are considered to be temperature independent.

Farris et al. (2011) proposed the mathematical model for predicting the human achilles tendon body core temperature during running. The RFA treatment region can be represented by an annulus with an imposed heat flux at the inner surface (the interface between the probe and the organ) and a body core temperature at the outer surface (the edge of the heated region). Fig. 1(b) illustrates a typical axisymmetric biological model including an ablation electrode (e.g. a heating probe) with a heat source along its shank. As seen, the cylindrical probe with a radius R_i, which is bounded by an annular treatment region, produces a constant heat flux q_w along the shank.

2.2. Governing equations

The anatomic structure is modeled as a porous medium consisting of the blood and tissue (solid matrix) phases. The governing energy equations for both phases incorporating internal heat generation (e.g. metabolic reactions) and LTNE condition can be represented as

Blood phase:

$$k_{b,eff}\frac{1}{r}\frac{\partial}{\partial r}\left(r\frac{\partial\langle T_b\rangle}{\partial r}\right)+h_{tb}a_{tb}\left(\langle T_t\rangle-\langle T_b\rangle\right)=\varepsilon\rho_b c_b\langle u\rangle\frac{\partial\langle T_b\rangle}{\partial z} \tag{1}$$

Tissue phase:

$$k_{t,eff}\frac{1}{r}\frac{\partial}{\partial r}\left(r\frac{\partial\langle T_t\rangle}{\partial r}\right)-h_{tb}a_{tb}\left(\langle T_t\rangle-\langle T_b\rangle\right)+(1-\varepsilon)Q_{met}=0 \tag{2}$$

where

$$k_{b,eff}=\varepsilon k_b+k_{b,dis} \tag{3}$$

$$k_{t,eff}=(1-\varepsilon)k_t \tag{4}$$

where r is the radial coordinate, $\langle T_b\rangle$, $\langle T_t\rangle$, $k_{b,eff}$, $k_{t,eff}$, $k_{b,dis}$, ε, ρ_b and c_b are the intrinsic phase average blood and tissue temperatures, blood and tissue effective thermal conductivities, blood dispersion thermal conductivity, porosity (the volume fraction of the vascular space), blood density and specific heat, respectively. The blood–tissue interfacial heat transfer coefficient is represented by h_{tb} and the specific surface area by a_{tb}, and Q_{met} is the metabolic heat generation.

2.3. Boundary conditions

Based on established results under LTNE condition in the literature (Lee and Vafai, 1999; Marafie and Vafai, 2001; Mahjoob and Vafai, 2009; Yang and Vafai, 2010), the imposed heat flux at the surface of heating probe can be represented as

$$q_w=-k_{b,eff}\frac{\partial\langle T_b\rangle}{\partial r}\bigg|_{r=R_i}-k_{t,eff}\frac{\partial\langle T_t\rangle}{\partial r}\bigg|_{r=R_i} \tag{5}$$

The temperature at the interface between the heating probe and the body organ is likely to be uniform regardless of whether it contacts the tissue solid matrix or the blood. As such, the tissue and blood temperatures at the probe–organ interface will be the same (Lee and Vafai, 1999; Marafie and Vafai, 2001; Mahjoob and Vafai, 2009, 2010).

$$\langle T_b\rangle|_{r=R_i}\approx\langle T_t\rangle|_{r=R_i}\approx T_w \tag{6}$$

The external heat flux generated by the heating probe influences the organ within a penetration depth of H. Here, $H=R_o-R_i$. On the outer surface the tissue and blood temperatures will be the same at the body core temperature at 37 °C (Giordano et al., 2010; Peng et al., 2011).

$$\langle T_b\rangle|_{r=R_o}\approx\langle T_t\rangle|_{r=R_o}\approx T_c=37\ ^oC \tag{7}$$

2.4. Normalization

To normalize the governing equations and boundary conditions, the dimensionless variables are introduced as follows

$$n=\frac{\eta_i}{\eta_o},\quad \eta_i=\frac{n}{1-n},\quad \eta_o=\frac{1}{1-n},\quad \eta=\frac{r}{H},\quad \kappa=\frac{k_{b,eff}}{k_{t,eff}},\quad Bi=\frac{h_{tb}a_{tb}H^2}{k_{t,eff}},$$
$$\theta_b=\frac{k_{t,eff}\left(\langle T_b\rangle-T_w\right)}{q_wH},\quad \theta_t=\frac{k_{t,eff}(\langle T_t\rangle-T_w)}{q_wH},\quad \Phi=\frac{(1-\varepsilon)\mathrm{HQ}_{met}}{q_w} \tag{8}$$

where κ is the ratio of the effective thermal conductivity of the blood to tissue and Bi the Biot number.

Adding the governing Eqs. (1) and (2), integrating the resultant equation over the cross-sectional area and applying boundary conditions given by Eqs. (5) and (7) leads to the following relationship

$$\varepsilon\rho_b c_b\langle u\rangle\frac{\partial\langle T_b\rangle}{\partial z}=\frac{2(n+\Gamma)q_w}{(1+n)H}+(1-\varepsilon)Q_{met} \tag{9}$$

where the derivative $\partial\langle T_b\rangle/\partial z$ is constant for thermally fully-developed flow, and

$$\Gamma=\frac{1}{q_w}\left(k_{b,\mathrm{eff}}\frac{\partial\langle T_b\rangle}{\partial r}+k_{t,eff}\frac{\partial\langle T_t\rangle}{\partial r}\right)\Bigg|_{r=R_o} \tag{10}$$

Considering the Darcy flow model and substituting Eqs. (8) and (9), the governing Eqs. (1) and (2) as well as boundary conditions (5) and (7) can be rewritten as

$$\kappa\frac{1}{\eta}\frac{\partial}{\partial\eta}\left(\eta\frac{\partial\theta_b}{\partial\eta}\right)+\mathrm{Bi}(\theta_t-\theta_b)=\frac{2(n+\Gamma)}{1+n}+\Phi \tag{11}$$

$$\frac{1}{\eta}\frac{\partial}{\partial\eta}\left(\eta\frac{\partial\theta_b}{\partial\eta}\right)-\mathrm{Bi}(\theta_t-\theta_b)+\Phi=0 \tag{12}$$

$$\theta_b|_{\eta=\eta_i}=\theta_t|_{\eta=\eta_i}=0 \tag{13}$$

$$\theta_b|_{\eta=\eta_o} = \theta_t|_{\eta=\eta_o} = \theta_c \tag{14}$$

where θ_c is the dimensionless core body temperature such that

$$\theta_c = \frac{k_{t,eff}(T_c - T_w)}{q_w H} \tag{15}$$

3. Analytical solution

3.1. Blood and tissue temperature distributions

The governing Eqs. (11) and (12) are solved analytically subject to the constant heat flux q_w at the inner surface and the constant temperature T_c at the outer surface. As such, the obtained blood and tissue temperature distributions may be employed to rewrite Eq. (10). In other words, the analytical solution to Eqs. (11) and (12) is independent of the term Γ (Mahjoob and Vafai, 2011). Following Mahjoob and Vafai (2011), the two governing Eqs. (11) and (12) are added to yield a new equation

$$\frac{1}{\eta}\frac{\partial}{\partial\eta}\left[\eta\frac{\partial}{\partial\eta}(\kappa\theta_b+\theta_t)\right] = \frac{2(n+\Gamma)}{1+n} \tag{16}$$

which is the second order Euler–Cauchy equation with the dependent variable $(\kappa\theta_b+\theta_t)$, which can be solved with the modified boundary conditions based on Eqs. (13) and (14) as

$$(\kappa\theta_b+\theta_t)|_{\eta=\eta_i} = 0 \tag{17}$$

$$(\kappa\theta_b+\theta_t)|_{\eta=\eta_o} = (1+\kappa)\theta_c \tag{18}$$

The complete solution for Eq. (16) is found to be

$$\kappa\theta_b+\theta_t = C_1 + C_2 ln\eta + \frac{(n+\Gamma)\eta^2}{2(1+n)} \tag{19}$$

where C_1 and C_2 denote the unknown constants illustrated in Appendix A [Eqs. A.1–A.6].

It is worth noting that θ_c on the outer surface is still unknown. The normalized form of Eq. (10), based on Eq. (8), can be written as

$$\Gamma = \kappa\frac{\partial\theta_b}{\partial\eta} + \frac{\partial\theta_t}{\partial\eta}|_{\eta=\eta_o} \tag{20}$$

Taking the derivative of both sides of Eq. (19) with respect to η and considering Eq. (20) lead to

$$\Gamma = C_2\frac{1}{\eta_o} + \frac{n+\Gamma}{1+n}\eta_o \tag{21}$$

Then, the solution for Γ can be easily obtained by solving Eq. (21), as illustrated in Appendix A [Eqs. A.7–A.9]. Rewriting Eq. (19) as

$$\theta_t = C_1 + C_2 ln\eta + \frac{(n+\Gamma)\eta^2}{2(1+n)} - \kappa\theta_b \tag{22}$$

and substituting it into Eq. (11) produces

$$\frac{1}{\eta}\frac{\partial}{\partial\eta}\left(\eta\frac{\partial\theta_b}{\partial\eta}\right) - \lambda^2\theta_b = -\frac{\mathrm{Bi}}{\kappa}\left[C_1 + C_2 ln\eta + \frac{n+\Gamma}{2(1+n)}\eta^2\right] + \frac{1}{\kappa}\left[\frac{2(n+\Gamma)}{1+n} + \Phi\right] \tag{23}$$

Eq. (23) is a modified Bessel equation. As such, we have decoupled Eqs. (11) and (12). Eq. (23) becomes a non-homogeneous ordinary differential equation which can be solved subject to the boundary conditions (13) and (14). As such, the complete solution takes the following form

$$\theta_b = D_1 I_0(\lambda\eta) + D_2 K_0(\lambda\eta) + D_3 ln\eta + D_4\eta^2 + D_5 \tag{24}$$

where $\lambda = \sqrt{(1+\kappa)Bi/\kappa}$ and I_0 and K_0 are the zeroth order modified Bessel functions of the first and second kind respectively. Substituting Eq. (24) into the boundary conditions given by Eqs. (13) and (14), one can obtain the unknown constants D_1, D_2, D_3, D_4 and D_5illustrated in Appendix A [Eqs. (A.10)–(A.24)]. It can be seen from Eqs. (A.1), (A.2) and (A.10)–(A.14), that all the constants are functions of the dimensionless core body temperature θ_c.

3.2. Determination of the dimensionless core body temperature

Once the dimensionless core body temperature θ_c on the outer surface is known, the expressions of Γ, C_1, C_2, D_1, D_2, D_3, D_4 and D_5 are explicitly obtained. For flow through an annular biological medium, the dimensionless bulk mean blood temperature averaged over the cross section is calculated as

$$\theta_{b,m} = \frac{2}{\eta_o^2-\eta_i^2}\int_{\eta_i}^{\eta_o}\theta_b\eta\, d\eta = \alpha_1 + \alpha_2\theta_c \tag{25}$$

where α_1 and α_2 are given in Appendix A [Eqs. A.25–A.30].

Integrating both sides of Eq. (9) simultaneously with regard to z results in

$$T_b = \frac{\frac{2(n+\Gamma)q_w}{(1+n)H} + (1-\varepsilon)Q_{met}}{\rho_b c_b u_e} z + \frac{q_w H}{k_{s,eff}}(\theta_f - \theta_{f,m}) + T_e \tag{26}$$

The dimensional bulk mean blood temperature can be defined as

$$T_{b,m} = \frac{2}{R_o^2-R_i^2}\int_{R_i}^{R_o} T_b r dr = \beta_1 + \beta_2\theta_c \tag{27}$$

where β_1 and β_2 are given in Appendix A [Eqs. A.31 and A.32].

From Eq. (15), we can obtain an expression for the dimensional temperature at the probe–organ interface as

$$T_w = T_c - \frac{q_w H}{k_{t,eff}}\theta_c \tag{28}$$

Similarly,

$$T_w = T_{b,m} - \frac{q_w H}{k_{t,eff}}\theta_{b,m} \tag{29}$$

Substitution of Eqs. (25), (27) and (28) into Eq. (29) leads to

$$T_c - \frac{q_w H}{k_{t,eff}}\theta_c = \beta_1 + \beta_2\theta_c - \frac{q_w H}{k_{t,eff}}(\alpha_1 + \alpha_2\theta_c) \tag{30}$$

Consequently, the dimensionless core body temperature θ_c can be obtained by solving Eq. (30) resulting in

$$\theta_c = \frac{q_w H\alpha_1 + k_{t,eff}(T_c - \beta_1)}{q_w H(1-\alpha_2) + k_{t,eff}\beta_2} \tag{31}$$

3.3. Heat transfer correlations

The probe–organ interface transfer coefficient for the local thermal non-equilibrium model is obtained from

$$h_w = \frac{q_w}{T_w - T_{b,m}} \tag{32}$$

After solving for the blood and tissue temperatures, the local Nusselt number,Nu, can be obtained from

$$\mathrm{Nu} = \frac{h_w(2H)}{k_{b,eff}} = -\frac{2}{\kappa\theta_{b,m}} \tag{33}$$

4. Results and discussion

4.1. Validation

Our analytical solutions are validated against very few existing exact solutions for the following three limiting cases: a parallel-plate channel subject to a heat flux on one surface and uniform core temperature on the other (Limiting case I) surface (Mahjoob and Vafai, 2009, 2010) or when subject to a heat flux on both

(Limiting case II) surfaces (Mahjoob and Vafai, 2009, 2010), and an annulus subject to a heat flux on the inner surface and an adiabatic condition on the outer (Limiting case III) surface (Qu et al., 2012). It should be noted that all the results are obtained at the entrance, i.e. $z=0$ unless otherwise stated.

4.1.1. Limiting case I ($\psi\to\infty,\Gamma\neq 0$)

Let us define $\psi=R_i/H$ as the aspect ratio of the annular geometry under consideration. As $\psi\to\infty$, the analytical solution within the annulus approaches that within the planar geometry (Mahjoob and Vafai, 2009, 2010). For purpose of plotting the results, typical values for the thermophysical properties are taken as: $k_b=0.45$ W/m °C, $k_t=0.54$ W/m °C, $c_b=3960$ J/kg °C and $\rho_b=1058\text{kg/m}^3$. The blood velocity and temperature at the entrance, metabolic heat generation, the imposed heat flux and the blood dispersion thermal conductivity are set to be $u_e=0.02$ m/s, $T_e=37$ °C, $Q_{met}=4200$ W/m^3, $q_w=200$ W/m^2 and $k_{b,dis}=0.006$ W/m °C, respectively. This yields $\Phi=0.189$ and $\kappa=0.105$. A representative volume fraction ($\varepsilon=0.1$) of the vascular system is employed for some of the comparisons (Mahjoob and Vafai, 2009). For the validation with the planar case, $R_i=10$ m and $R_o=10.01$ m are utilized, thus $H=0.01$ m and $\psi=1000$, to setup the present model to have approximately the same geometry and boundary conditions as that utilized by Mahjoob and Vafai (2009, 2010). As shown in Fig. 2(a), the present blood and tissue temperature distributions coincide very well with the results derived by Mahjoob and Vafai (2009, 2010).

4.1.2. Limiting case II ($\psi\to\infty,\Gamma=0$)

As mentioned in Mahjoob and Vafai (2011), Γ is represented by Eq. (10) for a constant temperature boundary condition while Γ is zero for an adiabatic boundary condition. To compare the present solution with the results for the limiting case II, herein we set $\Gamma=0$ and replace Eq. (14) by the following adiabatic boundary condition

$$\left.\frac{\partial\theta_b}{\partial\eta}\right|_{\eta=\eta_o}=\left.\frac{\partial\theta_t}{\partial\eta}\right|_{\eta=\eta_o}=0 \tag{34}$$

Using a similar approach as was used in deriving Eqs. (22) and (24), the solutions for Eqs. (11) and (12) subject to boundary conditions (13) and (34) are readily obtained, where are in the same form as those given by Eqs. (22) and (24), respectively. However, the involved constants C_1, C_2, D_1, D_2, D_3, D_4 and D_5 should be replaced with C_1', C_2', D_1', D_2', D_3', D_4' and D_5', which are given in Appendix A [Eqs. A.33–A.39]. For comparison purpose, the same geometric parameters as previous limiting case were used. Fig. 3(b) and (c) display the comparison for blood and tissue temperature distributions obtained by current analytical results with the ones obtained by Mahjoob and Vafai (2009, 2010). Once again, an excellent agreement can be observed. Also, the validation

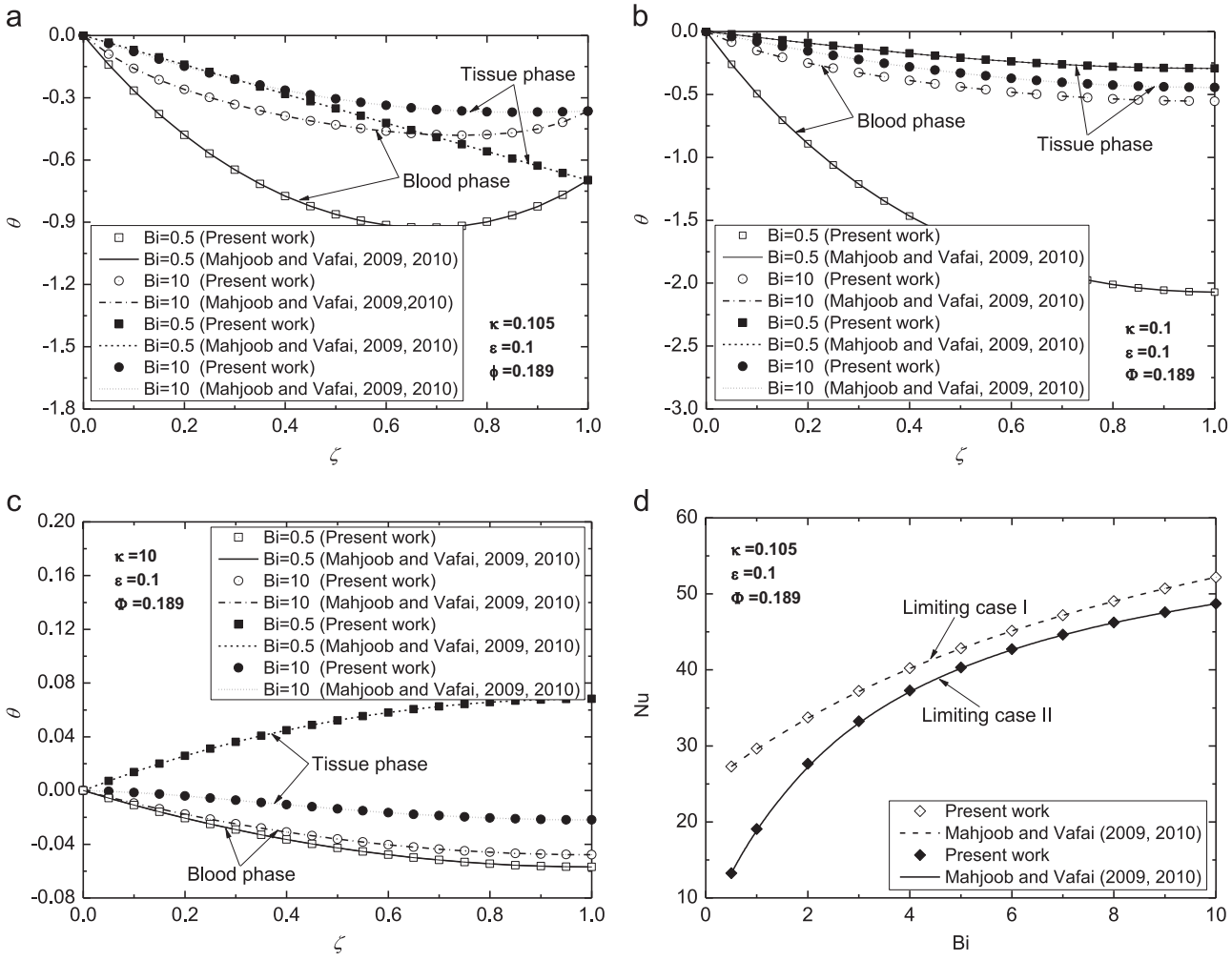

Fig. 2. Comparison of the present analytical solutions for (a) temperature (Limiting case I, $\kappa=0.105$), (b) temperature (Limiting case II, $\kappa=0.1$), (c) temperature (Limiting case II, $\kappa=10$), and (d) Nusselt number (Limiting cases I and II) with the results of Mahjoob and Vafai (2009, 2010).

of Nusselt number for both limiting cases I and II is depicted in Fig. 2(d).

4.1.3. *Limiting case III* ($\mathrm{Da}\to 0, \Gamma = 0$)

As the last limiting case, we consider an annulus with inner and outer radii $R_i = 0.01$ m and $R_o = 0.03$ m. As the Darcy number $\mathrm{Da}\to 0$, the Brinkman–Darcy extended flow model tends to Darcy flow model (Hooman and Ranjbar-Kani, 2004). To compare the present analytical solution with the work of Qu et al. (2012), the Darcy number is assumed to be small enough, say $\mathrm{Da} = 10^{-10}$. Fig. 3(a) and (b) shows the comparison of present temperature distributions with the ones given by Qu et al. (2012). Fig. 3(c) depicts the validation of the Nusselt number. All figures display an excellent agreement between the current results and those by Qu et al. (2012).

4.2. *Effect of physical parameters on the temperature distributions*

In what follows, based on physiological data, the inner and outer radii of the treatment region are taken as $R_i = 3\times 10^{-5}$ m and $R_o = 5\times 10^{-3}$ m. Fig. 4(a) illustrates the effect of metabolic heat generation on the blood and tissue temperature distributions for $\Phi = 0.01$, 0.1 and 0.5. The energy required for replenishment is produced by the oxidation of the nutrients supplied to the biological tissues. Any decrease in metabolic heat has to be compensated by an increase in the input energy to attain hyperthermia and vice versa. As expected, larger heat generation rate results in higher temperature in the tissue as well as the blood within it. Also, an increase in the metabolic heat generation rate enhances the temperature difference between the blood and tissue phases.

The vascular porosity, which increases with age (Norman et al., 2008), exhibits a wide range of values in human tissue, from 4% to more than 16% (Cardoso et al., 2013). Fig. 4(b) shows the effect of vascular volume fraction on the blood and tissue temperature distributions for $\varepsilon = 0.05$, 0.1 and 0.3. An increase in the volume fraction results in a more uniform temperature distribution, which possibly leads to a more effective hyperthermia treatment. It is worth noting that a change in the vascular volume fraction also translates in a change in the blood and tissue effective thermal conductivities. The natural body thermal regulation system increases or decreases the vascular volume fraction of the biological organ when exposed to a higher or lower temperature. This phenomenon has also been reported for surface heating by Mahjoob and Vafai (2009). It should be pointed out that the blood and tissue temperatures are within a relatively small range in certain physiological or medical situations. Therefore, the thermal properties of the biological bodies can be considered as constants.

Fig. 4(c) demonstrates the effect of the Biot number on the blood and tissue temperature distributions for $\mathrm{Bi} = 0.01$, 0.5, 10 and 50. It can be observed from this figure that the blood and tissue temperatures and their difference increases with a decrease in the Biot number. The reason is that when Bi is small, the internal heat

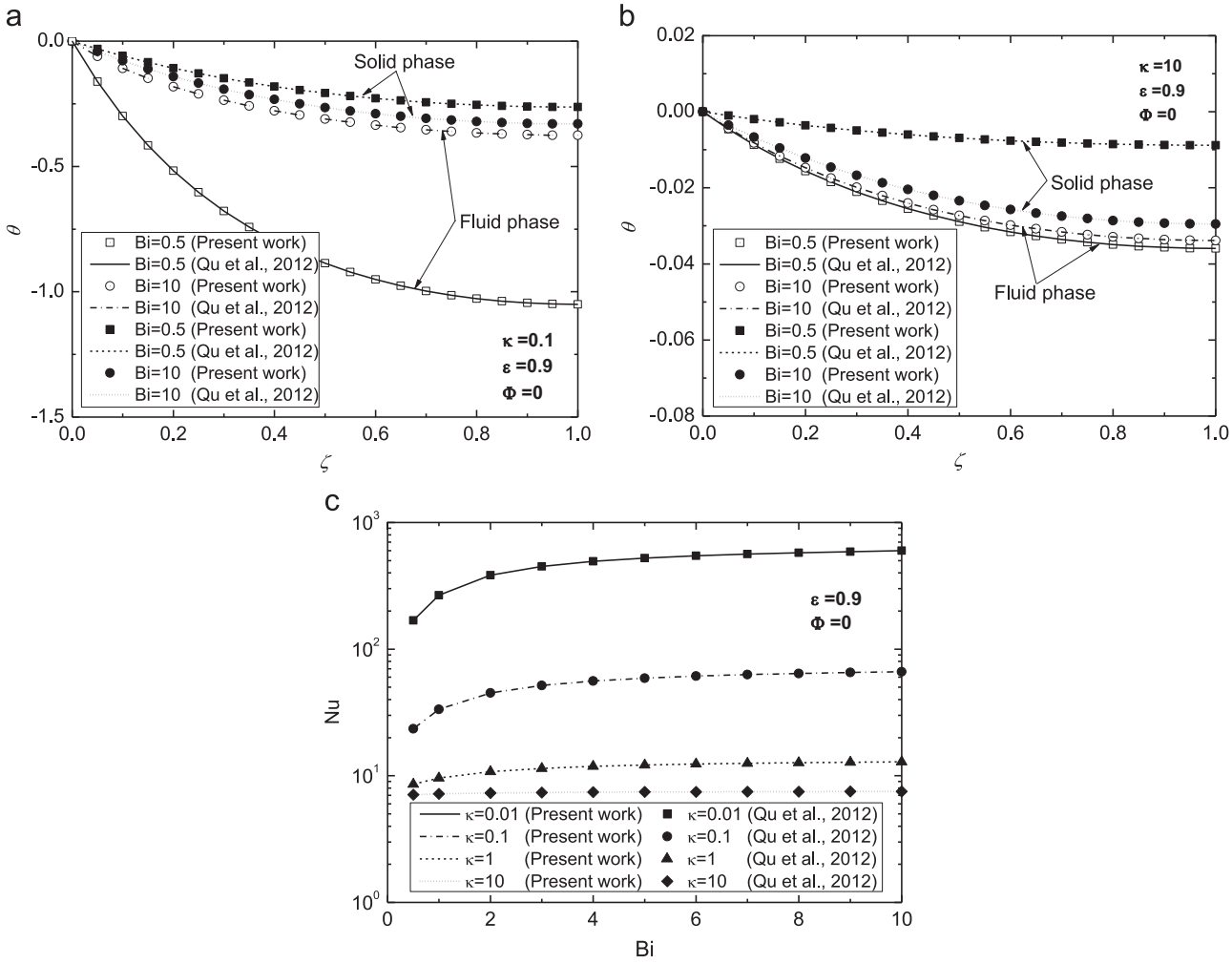

Fig. 3. Comparison of the present analytical solutions for (a) temperature (Limiting case III, $\kappa = 0.1$), (b) temperature (Limiting case III, $\kappa = 10$), and (c) Nusselt number (Limit case III) with the results of Qu et al. (2012).

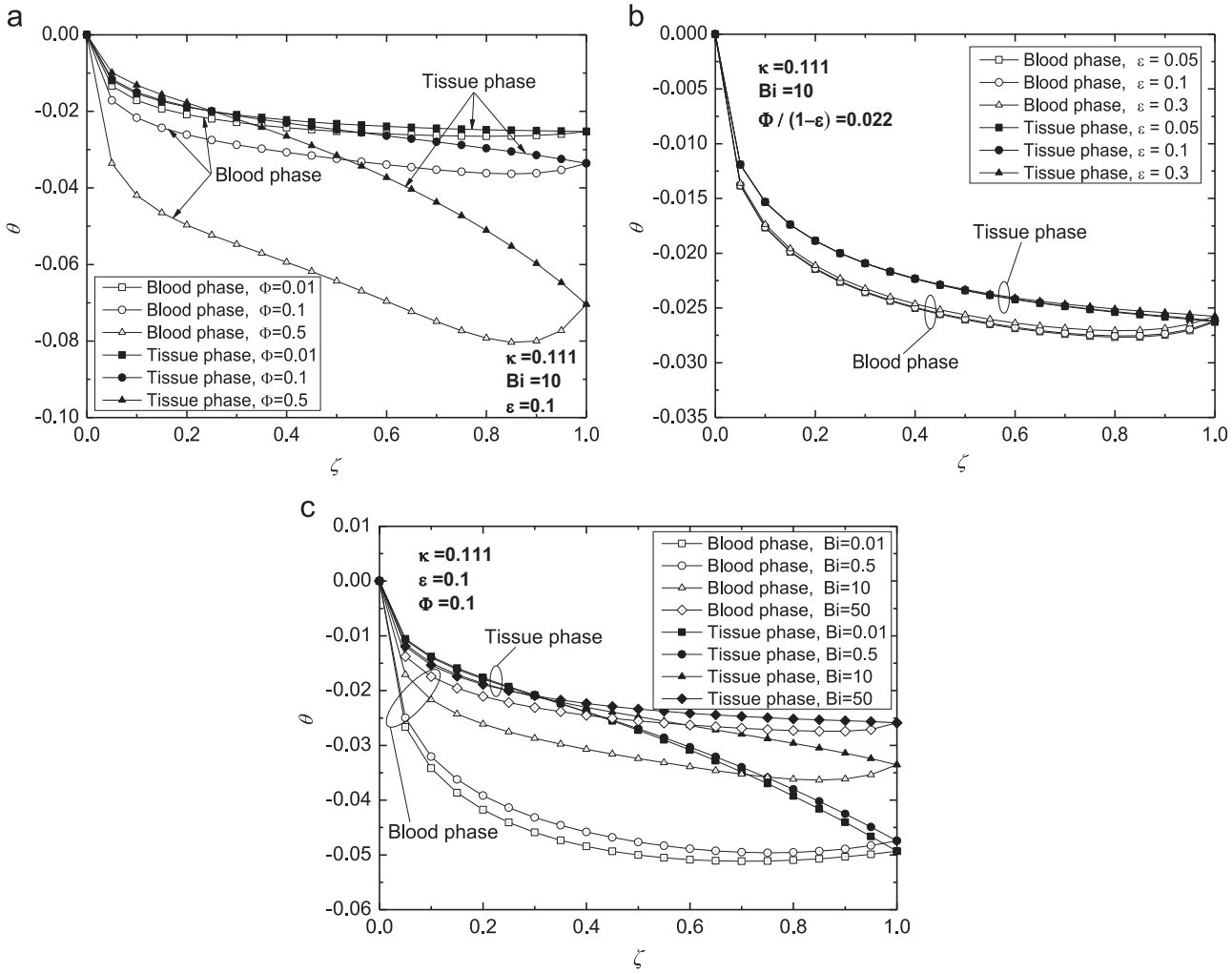

Fig. 4. Effects of (a) metabolic heat generation, (b) vascular volume fraction, and (c) Biot number on the blood and tissue temperature distributions.

transfer between the blood and tissue phases becomes relatively weak. Therefore, the blood perfusion cannot effectively remove the supplied energy during the probe based thermal therapy. In other words, smaller Bi is clinically helpful for improving the hyperthermia treatment effect.

Fig. 5(a) shows the impact of the effective thermal conductivity ratio on the blood and tissue temperature distributions for $\kappa=0.01$, 0.1, 1 and 10. A decrease in the effective thermal conductivity ratio results in an increase in the blood and tissue temperatures, due to a subsequent decrease in heat exchange between the probe surface and the blood. The analytical results presented in this study are applicable to thermal problems within several biological organs. Typical thermophysical properties of biological media (Bauman et al., 2004; He et al., 2008; Gilbert et al., 2009; Wessapan et al., 2011, 2012; Wessapan and Rattanadecho, 2012) are listed in Table 1. Here, the blood thermal dispersion effect can be represented by $k_{b,dis}=0.1\mathrm{PrRe}k_b$(Amiri and Vafai, 1994). This yields $\kappa=1.5008$, 0.2765, 1.2860, 3.3564 and 0.5742, respectively, for Liver, Brain, Cornea, Bone and Fat considered in our study. Fig. 5(b) displays the results incorporating the blood thermal dispersion for Bi=10 and $\Phi=0.1$. It is apparent that the blood and tissue temperatures within the Brain are higher than those within the other four biological media. This implies that the therapeutic heating can be more readily achieved within the Brain. As a point of comparison, the results without accounting for the blood thermal dispersion are also shown in the figure. When the thermal dispersion is not accounted for, the effective thermal conductivity ratio changes to $\kappa=1.3582$, 0.2103, 1.1638, 0.4190 and 3.0963 for the five biological media. As seen in Fig. 5(b), thermal dispersion reduces the blood and tissue temperatures, which translates into more required input energy to compensate for the decreased temperature arising from the blood dispersion.

Fig. 5(c) depicts the variation of blood and tissue temperature distributions at four axial locations along the z-axis with $\xi=z/H=0$, 10, 50 and 100. As expected, the temperature difference between blood and tissue reduces as ξ increases. When $\xi>0$, especially when $\xi\geq 50$, the temperature for both phases for $\zeta<0.6$ declines while that for $\zeta>0.6$ illustrates an opposite trend. When the probe shank is long enough, the temperatures in the vicinity of the probe surface will be relatively low while those near a healthy tissue will be relatively high. In such a situation, the tumor cells may not be efficiently treated but the normal tissue may be damaged due to the high temperature.

4.3. Establishing the criterion for simulation of a planar geometry to represent an annular one

As discussed earlier, if the aspect ratio ψ is set to be large enough the results for an annulus will match those obtained by the planar geometry. Here we seek to obtain the criterion for when the results obtained for the two geometries will match. For this purpose, the thickness of the annulus is kept unchanged, say $H=0.01$ m while the inner radius R_i varies starting from one times the thickness. In order to assess the matching of annular to planar

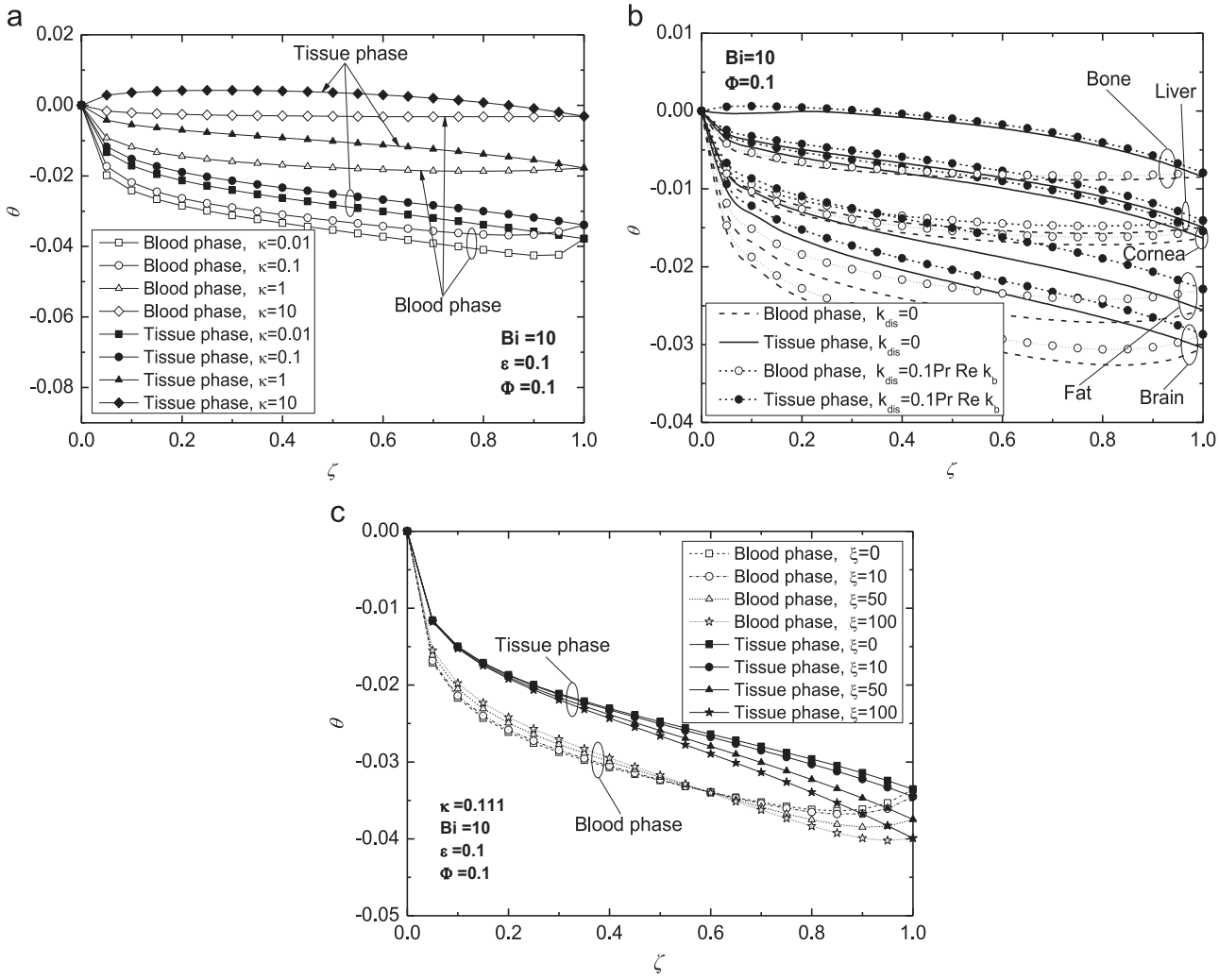

Fig. 5. (a) Effect of the effective thermal conductivity ratio on the blood and tissue temperature distributions, (b) the blood and tissue temperature distributions for different biological medias, and (c) their variation at different cross sections.

Table 1
Thermophysical properties of different biological media.

Biological materials	Density ρ(kg/m^3)	Thermal conductivity k (W/m °C)	Specific heat capacity c(J/kg °C)	Porosity (ε)
Liver	1030	0.497	3600	0.6
Brain	1038	0.535	3650	0.2
Cornea	1050	0.58	4178	0.6
Bone	1038	0.436	3437	0.2
Fat	916	0.22	2300	0.75
Blood	1058	0.45	3960	1.0

geometries, the following criterion is employed

$$E=\left|\frac{\theta_a-\theta_p}{\theta_p}\right| \times 100\% \rightarrow 1\% \tag{35}$$

where θ_a and θ_p are the dimensionless temperatures in the annular and planar geometries respectively and E is the relative error obtained by analytical temperatures in the annular and planar geometries.

The calculated results for E in the present study and Eqs. (33) and (34) of Mahjoob and Vafai (2009) are tabulated for two locations along the r-axis. In Table 2, the first data corresponding to each ψ is for the blood phase and the second one is for the tissue phase. It is evident from this table that the relative error

Table 2
Relative errors for the blood and tissue temperatures at selected points.

ψ	$\kappa=0.1$, $Bi=0.5$		$\kappa=0.1$, $Bi=10$		$\kappa=10$, $Bi=0.5$		$\kappa=10$, $Bi=10$	
	$\eta=0.5$	$\eta=0.75$	$\eta=0.5$	$\eta=0.75$	$\eta=0.5$	$\eta=0.75$	$\eta=0.5$	$\eta=0.75$
1	26.730	26.903	14.675	15.071	9.688	9.967	9.622	9.859
	10.865	16.857	9.251	10.778	73.812	8.652	4.644	5.282
10	3.795	3.836	1.709	1.757	1.034	1.096	1.027	1.070
	0.984	1.953	0.876	1.086	14.437	2.267	0.143	0.268
20	1.945	1.967	0.862	0.886	0.518	0.551	0.522	0.538
	0.483	0.982	0.434	0.541	7.513	1.197	0.057	0.122
30	1.307	1.322	0.576	0.592	0.346	0.368	0.353	0.359
	0.320	0.656	0.289	0.360	5.077	0.812	0.035	0.079
40	0.985	0.996	0.433	0.445	0.260	0.276	0.268	0.270
	0.239	0.493	0.216	0.270	3.834	0.614	0.025	0.058
50	0.790	0.799	0.347	0.356	0.208	0.221	0.218	0.216
	0.191	0.394	0.173	0.216	3.079	0.495	0.020	0.046
100					0.104	0.111	0.116	0.108
					1.552	0.250	0.009	0.022
150					0.069	0.074	0.082	0.072
					1.038	0.108	0.006	0.014
200					0.052	0.055	0.065	0.054
					0.779	0.126	0.005	0.011

decreases with an increase in ψ. The maximum relative errors corresponding to $\psi=150$ and 200 are 1.038% and 0.779% respectively. Moreover, it is found that the value of the relative error decreases linearly from $\psi=100$, 150 to 200. Therefore, the minimum aspect ratio $\psi_{\min}=157$ can be obtained by linear interpolation between $\psi=150$ and 200. In practice, a conservative value of $\psi=160$ may be employed to predict, at least for the case of *Bi* ranging from 0.5 to 10 and κ from 0.1 to 10, the behavior of bioheat transport in planar geometry addressed by Mahjoob and Vafai (2009). Thus, a relationship between annular and planar geometries has been constructed through the aspect ratio of the annulus. This implies the similarity between deep heating and surface heating in certain conditions.

5. Conclusions

Understanding and predicting heat transport and temperature distribution inside biological media are crucial in hyperthermia treatments such as RFA. In this work, analytical solutions are established for the blood and tissue temperature distributions as well as the overall heat exchange correlations. Our analytical results were comprehensively validated. The derived analytical solutions provide general characteristics of the bioheat transfer during a RFA treatment. The effects of physiological parameters such as metabolic heat generation, volume fraction of the vascular space, ratio of the effective blood to tissue conductivities, etc., were analyzed in this work. An increase in the metabolic heat generation or in the vascular volume fraction enhances the temperatures for the blood and tissue phases. When $\xi>0$, especially when $\xi\geq 5$, the blood and tissue temperatures for $\zeta<0.6$ decline while those for $\zeta>0.6$ illustrate an opposite trend. The obtained analytical results enable the clinicians to predict the temperature distribution in a biological medium within a real time feedback mechanism. Based on the present solutions, an approach to optimize the hyperthermia parameters can be obtained for the tumor destroying temperature and tissue burn threshold. Finally, a criterion for simulation of a planar geometry to represent an annular one is established.

As reported by many investigators, the mechanical properties of treated tissues will change after a thermal therapy and, in turn, affect the post-treatment structural integrity and functions of the tissue (Chen and Humphrey, 1998; Qian et al, 2013). Lin et al. (2012) found that the Young's modulus and stiffness of skin tissue decreased with increasing heating temperature, which was correlated to the skin microstructure changes induced by thermal denaturation. Therefore, the present analytical results enable the researchers to better understand the effect of post-treatment of treated tissues or organs on their structural integrity and hence more effectively design the clinical therapy protocols.

Conflict of interest statement

None.

Acknowledgments

This work was supported by the Visiting Scholar Program for Young Faculty in Shanghai, China. The authors would like to acknowledge this support.

Appendix A

The constants involved in Eq. (19) are given by

$$C_1=C_{11}+C_{12}\theta_c \tag{A.1}$$

$$C_2=C_{21}+C_{22}\theta_c \tag{A.2}$$

where

$$C_{11}=\frac{n+\Gamma_1}{2(1+n)}\frac{\eta_i^2\ ln\ \eta_o-\eta_o^2\ ln\ \eta_i}{ln\ \eta_i-\ ln\ \eta_o} \tag{A.3}$$

$$C_{12}=\frac{1}{ln\eta_i-ln\eta_o}\left[(1+\kappa)ln\eta_i+\frac{\Gamma_2}{2(1+n)}(\eta_i^2 ln\eta_o-\eta_o^2 ln\eta_i)\right] \tag{A.4}$$

$$C_{21}=\frac{n+\Gamma_1}{2(1+n)}\frac{\eta_o^2-\eta_i^2}{ln\eta_i-ln\eta_o} \tag{A.5}$$

$$C_{22}=\frac{1}{ln\eta_i-ln\eta_o}\left[-(1+\kappa)+\frac{\Gamma_2}{2(1+n)}(\eta_o^2-\eta_i^2)\right] \tag{A.6}$$

The expression for Γ is given by

$$\Gamma=\Gamma_1+\Gamma_2\theta_c \tag{A.7}$$

where

$$\Gamma_1=\frac{n(1+2ln\eta_i-2ln\eta_o)\eta_o^2-n\eta_i^2}{\eta_i^2+\eta_o[2(1+n)(ln\eta_i-ln\eta_o)-(1+2ln\eta_i-2ln\eta_o)\eta_o]} \tag{A.8}$$

$$\Gamma_2=\frac{-2(1+\kappa)(1+n)}{\eta_i^2+\eta_o[2(1+n)(ln\eta_i-ln\eta_o)-(1+2ln\eta_i-2ln\eta_o)\eta_o]} \tag{A.9}$$

The constants D_1, D_2, D_3, D_4 and D_5 involved in Eq. (24) are given by

$$D_1=D_{11}+D_{12}\theta_c \tag{A.10}$$

$$D_2=D_{21}+D_{22}\theta_c \tag{A.11}$$

$$D_3=D_{31}+D_{32}\theta_c \tag{A.12}$$

$$D_4=D_{41}+D_{42}\theta_c \tag{A.13}$$

$$D_5=D_{51}+D_{52}\theta_c \tag{A.14}$$

where

$$D_{11}=\frac{K_0(\lambda\eta_o)(D_{31}ln\eta_i+D_{41}\eta_i^2+D_{51})-K_0(\lambda\eta_i)(D_{31}ln\eta_o+D_{41}\eta_o^2+D_{51})}{I_0(\lambda\eta_o)K_0(\lambda\eta_i)-I_0(\lambda\eta_i)K_0(\lambda\eta_o)} \tag{A.15}$$

$$D_{12}=\frac{K_0(\lambda\eta_o)(D_{32}ln\eta_i+D_{42}\eta_i^2+D_{52})-K_0(\lambda\eta_i)(D_{32}ln\eta_o+D_{42}\eta_o^2+D_{52}-1)}{I_0(\lambda\eta_o)K_0(\lambda\eta_i)-I_0(\lambda\eta_i)K_0(\lambda\eta_o)} \tag{A.16}$$

$$D_{21}=\frac{-I_0(\lambda\eta_o)(D_{31}ln\eta_i+D_{41}\eta_i^2+D_{51})+I_0(\lambda\eta_i)(D_{31}ln\eta_o+D_{41}\eta_o^2+D_{51})}{I_0(\lambda\eta_o)K_0(\lambda\eta_i)-I_0(\lambda\eta_i)K_0(\lambda\eta_o)} \tag{A.17}$$

$$D_{22}=\frac{-I_0(\lambda\eta_o)(D_{32}ln\eta_i+D_{42}\eta_i^2+D_{52})+I_0(\lambda\eta_i)(D_{32}ln\eta_o+D_{42}\eta_o^2+D_{52}-1)}{I_0(\lambda\eta_o)K_0(\lambda\eta_i)-I_0(\lambda\eta_i)K_0(\lambda\eta_o)} \tag{A.18}$$

$$D_{31}=\frac{C_{21}}{1+\kappa} \tag{A.19}$$

$$D_{32}=\frac{C_{22}}{1+\kappa} \tag{A.20}$$

$$D_{41}=\frac{n+\Gamma_1}{2(1+\kappa)(1+n)} \tag{A.21}$$

$$D_{42}=\frac{\Gamma_2}{2(1+\kappa)(1+n)} \tag{A.22}$$

$$D_{51}=\frac{C_{11}}{1+\kappa}+\frac{4D_{41}}{\lambda^2}-\frac{1}{(1+\kappa)Bi}\left[\frac{2(n+\Gamma_1)}{1+n}+\Phi\right] \tag{A.23}$$

$$D_{52}=\frac{C_{12}}{1+\kappa}+\frac{4D_{42}}{\lambda^2}-\frac{1}{(1+\kappa)\mathrm{Bi}}\left(\frac{2\Gamma_2}{1+n}+\Phi\right) \tag{A.24}$$

The expressions for α_1 and α_2 involved in Eq. (25) are given by

$$\alpha_1=P_1D_{11}+P_2D_{21}+P_3D_{31}+P_4D_{41}+D_{51} \tag{A.25}$$

$$\alpha_2=P_1D_{12}+P_2D_{22}+P_3D_{32}+P_4D_{42}+D_{52} \tag{A.26}$$

where

$$P_1=\frac{2\left[\eta_oI_1(\lambda\eta_o)-\eta_iI_1(\lambda\eta_i)\right]}{\lambda\left(\eta_o^2-\eta_i^2\right)} \tag{A.27}$$

$$P_2=\frac{2\left[\eta_iK_1(\lambda\eta_i)-\eta_oK_1(\lambda\eta_o)\right]}{\lambda\left(\eta_o^2-\eta_i^2\right)} \tag{A.28}$$

$$P_3=\frac{\eta_o^2ln\eta_o-\eta_i^2ln\eta_i}{\eta_o^2-\eta_i^2}-\frac{1}{2} \tag{A.29}$$

$$P_4=\frac{\eta_o^2+\eta_i^2}{2} \tag{A.30}$$

Here, I_1 and K_1 are the first order modified Bessel functions of the first and second kind.

The expressions for β_1 and β_2 involved in Eq. (27) are given by

$$\beta_1=\frac{2(n+\Gamma_1)+(1+n)\Phi}{(1+n)\rho_bc_bu_eH/q_w}z+T_e \tag{A.31}$$

$$\beta_2=\frac{2\Gamma_2}{(1+n)\rho_bc_bu_eH/q_w}z \tag{A.32}$$

When making a comparison with the work by Qu et al. (2012), the constants C_1, C_2, D_1, D_2, D_3, D_4 and D_5 in Eqs. (22) and (24) should be replaced with C_1', C_2', D_1', D_2', D_3', D_4' and D_5', which are given by [see Section 4.1.2]

$$C_1'=\frac{n\left(2\eta_o^2ln\eta_i-\eta_i^2\right)}{2(1+n)} \tag{A.33}$$

$$C_2'=-\frac{n\,\eta_o^2}{1+n} \tag{A.34}$$

$$D_1'=-\frac{K_1(\lambda\eta_o)\left(D_3'ln\eta_i+D_4'\eta_i^2+D_5'\right)+\frac{1}{\lambda}K_0(\lambda\eta_i)\left(\frac{D_3'}{\eta_o}+2D_4'\eta_o\right)}{I_1(\lambda\eta_o)K_0(\lambda\eta_i)+I_0(\lambda\eta_i)K_1(\lambda\eta_o)} \tag{A.35}$$

$$D_2'=-\frac{I_1(\lambda\eta_o)\left(D_3'ln\eta_i+D_4'\eta_i^2+D_5'\right)-\frac{1}{\lambda}I_0(\lambda\eta_i)\left(\frac{D_3'}{\eta_o}+2D_4'\eta_o\right)}{I_1(\lambda\eta_o)K_0(\lambda\eta_i)+I_0(\lambda\eta_i)K_1(\lambda\eta_o)} \tag{A.36}$$

$$D_3'=\frac{C_2'}{1+\kappa} \tag{A.37}$$

$$D_4'=\frac{n}{2(1+\kappa)(1+n)} \tag{A.38}$$

$$D_5'=\frac{C_1'}{1+\kappa}+\frac{4D_4'}{\lambda^2}-\frac{1}{(1+\kappa)\mathrm{Bi}}\left(\frac{2n}{1+n}+\Phi\right) \tag{A.39}$$

In the above equations the prime superscript is indicative of the new values of the constants given in Eqs. (A.1), (A.2) and (A.10)–(A.14).

References

Alazmi, B., Vafai, K., 2000. Analysis of variants within the porous media transport models. J. Heat Transf. 122, 303–326.

Amiri, A., Vafai, K., 1994. Analysis of dispersion effects and non-thermal equilibrium, non-Darcian, variable porosity incompressible flow through porous media. Int. J. Heat Mass Transf. 37, 939–954.

Bauman, M.A., Gillies, G.T., Raghavan, R., Brady, M.L., Pedain, C., 2004. Physical characterization of neurocatheter performance in a brain phantom gelatin with nanoscale porosity: steady-state and oscillatory flows. Nanotechnol. 15, 92–97.

Boronyak, S.M., Merryman, W.D., 2014. In vitro assessment of a combined radio-frequency ablation and cryo-anchoring catheter for treatment of mitral valve prolapse. J. Biomech. 47, 973–980.

Cardoso, L., Fritton, S.P., Gailani, G., Benalla, M., Cowin, S.C., 2013. Advances in assessment of bone porosity, permeability and interstitial fluid flow. J. Biomech. 46, 253–265.

Chen, S.S., Humphrey, J.D., 1998. Heat-induced changes in the mechanics of a collagenous tissue: pseudoelastic behavior at 37 °C. J. Biomech. 31, 211–216.

Chua, K.J., Chou, S.K., Ho, J.C., 2007. An analytical study on the thermal effects of cryosurgery on selective cell destruction. J. Biomech. 40, 100–116.

Chung, S., Vafai, K., 2014. Mechanobiology of low-density lipoprotein transport within an arterial wall–Impact of hyperthermia and coupling effects. J. Biomech. 47, 137–147.

Cookson, A.N., Lee, J., Michler, C., Chabiniok, R., Hyde, E., Nordsletten, D.A., Sinclair, M., Siebes, M., Smith, N.P., 2012. A novel porous mechanical framework for modelling the interaction between coronary perfusion and myocardial mechanics. J. Biomech. 45, 850–855.

Dombrovsky, L.A., Randrianalisoa, J.H., Lipinsk, W., Timchenko, V., 2013. Simplified approaches to radiative transfer simulations in laser-induced hyperthermia of superficial tumors. Comput. Therm. Sci. 5, 521–530.

Dombrovsky, L.A., Timchenko, V., Jackson, M., 2012. Indirect heating strategy for laser induced hyperthermia: an advanced thermal model. Int. J. Heat Mass Transf. 55, 4688–4700.

Farris, D.J., Trewartha, G., McGuigan, M.P., 2011. Could intra-tendinous hyperthermia during running explain chronic injury of the human Achilles tendon? J. Biomech. 44, 822–826.

Field, S.B., 1987. Hyperthermia in the treatment of cancer. Phys. Med. Biol. 32, 789–811.

Gilbert, R.P., Liu, Y., Groby, J.P., Ogam, E., Wirgin, A., Xu, Y., 2009. Computing porosity of cancellous bone using ultrasonic waves, II: The muscle, cortical, cancellousbone system. Math. Comput. Model. 50, 421–429.

Giordano, M.A., Gutierrez, G., Rinaldi, C., 2010. Fundamental solutions to the bioheat equation and their application to magnetic fluid hyperthermia. Int. J. Hyperth. 26, 475–484.

Goldberg, N., Gazelle, S., Mueller, P., 2000. Thermal ablation therapy for focal malignancy: a unified approach to underlying principles, techniques, and diagnostic imaging guidance. Am. J. Roentgenol. 174, 323–331.

He, Y., Liu, H., Himeno, R., Sunaga, J., Kakusho, N., Yokota, H., 2008. Finite element analysis of blood flow and heat transfer in an image-based human finger. Comput. Biol. Med. 38, 555–562.

Hooman, K., Ranjbar-Kani, A.A., 2004. A perturbation based analysis to investigate forced convection in a porous saturated tube. J. Comput. Appl. Math. 162, 411–419.

Keangin, P., Rattanadecho, P., 2013. Analysis of heat transport on local thermal non-equilibrium in porous liver during microwave ablation. Int. J. Heat Mass Transf. 67, 46–60.

Keangin, P., Vafai, K., Rattanadecho, P., 2013. Electromagnetic field effects on biological materials. Int. J. Heat Mass Transf. 65, 389–399.

Khaled, A.R.A., Vafai, K., 2003. The role of porous media in modeling flow and heat transfer in biological tissues. Int. J. Heat Mass Transf. 46, 4989–5003.

Khanafer, K., Vafai, K., 2006. The role of porous media in biomedical engineering as related to magnetic resonance imaging and drug delivery. Heat Mass Transf. 42, 939–953.

Khanafer, K., Vafai, K., 2009. Synthesis of mathematical models representing bioheat transport. Adv. Numer. Heat Transf. 3, 1–28.

Kiss, M.Z., Daniels, M.J., Varghese, T., 2009. Investigation of temperature-dependent viscoelastic properties of thermal lesions in ex vivo animal liver tissue. J. Biomech. 42, 959–966.

Lee, D.Y., Vafai, K., 1999. Analytical characterization and conceptual assessment of solid and fluid temperature differentials in porous media. Int. J. Heat Mass Transf. 42, 423–435.

Lin, M., Zhai, X., Wang, S.Q., Wang, Z.J., Xu, F., Lu, T.J., 2012. Influences of supra-physiological temperatures on microstructure and mechanical properties of skin tissue. Med. Eng. Phys. 34, 1149–1156.

Liu, J., 2001. Uncertainty analysis for temperature prediction of biological bodies subject to randomly spatial heating. J. Biomech. 34, 1637–1642.

Mahjoob, S., Vafai, K., 2009. Analytical characterization of heat transfer through biological media incorporating hyperthermia treatment. Int. J. Heat Mass Transf. 52, 1608–1618.

Mahjoob, S., Vafai, K., 2010. Analysis of bioheat transport through a dual layer biological media. J. Heat Transf. 132, 031101.1–031101.14.

Mahjoob, S., Vafai, K., 2011. Analysis of heat transfer in consecutive variable cross sectional domains – applications in biological media and thermal management. J. Heat Transf. 133, 011006.1–011006.9.

Marafie, A., Vafai, K., 2001. Analysis of non-Darcian effects on temperature differentials in porous media. Int. J. Heat Mass Transf. 44, 4401–4411.

Nakayama, A., Kuwahara, F., 2008. A general bioheat transfer model based on the theory of porous media. Int. J. Heat Mass Transf. 51, 3190–3199.

Norman, T.L., Little, T.M., Yeni, Y.N., 2008. Age-related changes in porosity and mineralization and in-service damage accumulation damage accumulation. J. Biomech. 41, 2868–2873.

Peng, T., O'Neill, D.P., Payne, S.J., 2011. A two-equation coupled system for determination of liver tissue temperature during thermal ablation. Int. J. Heat Mass Transf. 54, 2100–2109.

Qian, N.S., Liao, Y.H., Cai, S.W., Raut, V., Dong, J.H., 2013. Comprehensive application of modern technologies in precise liver resection. Hepatobiliary Pancreat. Dis. Int. 12, 244–250.

Qu, Z.G., Xu, H.J., Tao, W.Q., 2012. Fully developed forced convective heat transfer in an annulus partially filled with metallic foams: an analytical solution. Int. J. Heat Mass Transf. 55, 7508–7519.
Rattanadecho, P., Keangin, P., 2013. Numerical study of heat transfer and blood flow in two-layered porous liver tissue during microwave ablation process using single and double slot antenna. Int. J. Heat Mass Transf. 58, 457–470.
Wessapan, T., Rattanadecho, P., 2012. Specific absorption rate and temperature increase in human eye subjected to electromagnetic fields at 900 MHz. J. Heat Transf. 134, 91101.1–91101.11.
Wessapan, T., Srisawatdhisukul, S., Rattanadecho, P., 2011. Numerical analysis of specific absorption rate and heat transfer in the human body exposed to leakage microwave power at 915 MHz and 2450 MHz. J. Mass Transf. 133, 051101.1–051101.13.
Wessapan, T., Srisawatdhisukul, S., Rattanadecho, P., 2012. Specific absorption rate and temperature distributions in human head subjected to mobile phone radiation at different frequencies. Int. J. Heat Mass Transf. 55, 347–359.
Wu, J., Long, Q., Xu, S.X., Anwar, R., Padhani, A.R., 2009. Study of tumor blood perfusion and its variation due to vascular normalization by anti-angiogenic therapy based on 3D angiogenic microvasculature. J. Biomech. 42, 712–721.
Xuan, Y., Roetzel, W., 1997. Bioheat equation of the human thermal system. Chem. Eng. Technol. 20, 268–276.
Yang, K., Vafai, K., 2010. Analysis of temperature gradient bifurcation in porous media-An exact solution. Int. J. Heat Mass Transf. 53, 4316–4325.
Zhang, Y.W., 2009. Generalized dual-phase lag bioheat equations based on nonequilibrium heat transfer in living biological tissues. Int. J. Heat Mass Transf. 52, 4829–4834.